


Wireless power transfer in magnetic resonance imaging at a higher-order mode of a birdcage coil

Oleg I. Burmistrov^{✉,*}, Nikita V. Mikhailov[✉], Dmitriy S. Dashkevich, Pavel S. Seregin, and Nikita A. Olekhno[✉]

School of Physics and Engineering, ITMO University, 49 Kronverksky pr., bldg. A, Saint Petersburg 197101, Russia

 (Received 28 August 2023; revised 23 November 2023; accepted 14 December 2023; published 24 January 2024)

Magnetic resonance imaging (MRI) is a crucial tool for medical visualization. In many cases, performing a scanning procedure requires the use of additional equipment, which can be powered by wires as well as via wireless power transfer (WPT) or wireless energy harvesting. In this study, we propose a scheme for WPT that uses a higher-order mode of the birdcage coil of the MRI scanner for energy transmission. In contrast to the existing WPT solutions, our approach does not require additional transmitting coils. Compared to energy harvesting, the proposed method allows the supply of significantly more power. We perform numerical simulations demonstrating that one can use the fundamental mode of the birdcage coil to perform a scanning procedure while transmitting the energy to the receiver at a higher-order mode without any interference with the scanning signal or violation of safety constraints, as guaranteed by the mode structure of the birdcage. Also, we evaluate the specific absorption rate along with the energy-transfer efficiency and verify our numerical model by a direct comparison with an experimental setup featuring a birdcage coil of a 1.5-T MRI scanner.

DOI: [10.1103/PhysRevApplied.21.014047](https://doi.org/10.1103/PhysRevApplied.21.014047)

I. INTRODUCTION

Magnetic resonance imaging (MRI) [1] has become one of the key medical visualization tools. MRI scanning procedures often rely on additional transmit and receive local coils, heart-activity monitors, and other equipment placed near the patient inside an MRI scanner bore [2] [Fig. 1(a)]. Typically, such devices are powered via special cables. However, such cables are bulky and may create imaging artifacts [2], reduce the patient's comfort, or even lead to thermal injuries [3,4]. The other approach is based on wireless energy transmission methods, including two groups: wireless power transfer (WPT) [5–8] and wireless energy harvesting (WEH) [9–13]. Despite applications of WPT [14–16] and WEH [17–20] being widely developed in other areas, they possess certain limitations.

The choice of an appropriate method depends on various factors, including the required transferred power level and the MRI scanner configuration. WPT allows the transmission of higher power levels but requires the presence of an additional transmitting antenna, typically not included in standard MRI scanner configurations. Besides, locating a transmitting WPT antenna inside a scanner bore is difficult due to the lack of free space and challenges in electromagnetic compatibility. On the other hand, WEH

does not require an additional transmitting antenna inside a scanner bore, as it relies on converting a part of the excitation radio-frequency (rf) pulse energy at the fundamental mode frequency of a body coil. However, the harvesting allows the collection of only low power levels, which are suitable for powering various simple sensors requiring milliwatt power levels [9,13] but are unlikely to supply more complex equipment. Such examples include readily manufactured multichannel wireless local coils requiring 1–2 W per channel [2], as well as solutions in development, such as Lorentz-force-actuated needle positioners [21,22] and wireless-orientation-locking capsule robots [23]. Moreover, the received power for the harvesting depends on the applied pulse sequence [13]. Besides, WEH [9,10,13] can considerably distort the rf excitation field and decrease the quality of MR images compared to WPT [5–7], which uses a different frequency compared to the scanning frequency.

In this paper, we propose a scheme for wireless power transfer in 1.5-T MRI that does not require the use of additional transmitting coils. In particular, we consider the modes of a birdcage coil [24,25]—one of the most popular solutions for rf body coils in 1.5-T setups—and demonstrate that one can implement WPT at higher-order modes of the birdcage (which typically are not excited in MRI scanners) while performing the scanning routine at the fundamental mode [Figs. 1(a) and 1(b)], in contrast to previous schemes implementing WPT at the fundamental mode

*oleg.burmistrov@metalab.ifmo.ru

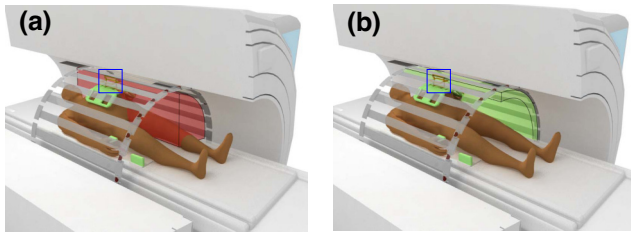


FIG. 1. A sketch of WPT in an MRI setup, demonstrating the patient located on the table inside the MRI scanner bore, local coils and medical sensors (green), and the birdcage coil (gray). The birdcage creates an rf magnetic field either at (a) the fundamental mode (shaded in red) or (b) the higher-order mode (shaded in green). A receiving system (shown with a blue frame) is located atop the patient.

[26]. The fundamental mode is characterized by a uniform distribution of the rf field B_1^+ inside the bore, which is used to excite nuclear magnetic resonance [Fig. 1(a)]. As we demonstrate further, electromagnetic fields of higher-order modes concentrate in the vicinity of the bore surface, i.e., in the area where potential receivers are placed, and are nearly absent in the central region where the patient is located [Fig. 1(b)]. However, WPT at a higher-order mode can be implemented only within the transmit mode of the scanning procedure, because a body coil is typically detuned while receiving the B_1^- field if a local coil is used during the scan [25].

The paper is organized as follows. In Sec. II, we outline the proposed scheme and describe the details of its numerical model. Section III includes the results of numerical simulations for the spectrum and field distributions of different higher-order modes of the birdcage coil, as well as the evaluation of the WPT efficiency. Then, in Sec. IV, we provide details of experimental studies that verify the numerical results. Section V contains a discussion and final remarks.

II. NUMERICAL MODEL

A typical structure of a high-pass birdcage coil is shown in Fig. 2(a). We consider a coil consisting of $N = 16$ copper strips placed at the side surface of a cylinder and connected by capacitors. The complete schematics are given in the Supplemental Material [27]. The diameter of the coil is 636 mm and the length is 575 mm. Such parameters correspond to the geometry and sizes of the Siemens Avanto 1.5-T body coil. The numerical model includes two ports [red markers in Fig. 2(a)], connecting the first and the fifth strips of the birdcage with the surrounding electromagnetic shield, and the phantom, which emulates the load created by a patient inside the scanner [Fig. 2(a)]. The diameter of the phantom is 300 mm, the length is 500 mm, the permittivity is $\epsilon = 80$, and the conductivity is 1 Sm/m, corresponding to standard MRI Siemens phantom at 1.5 T.

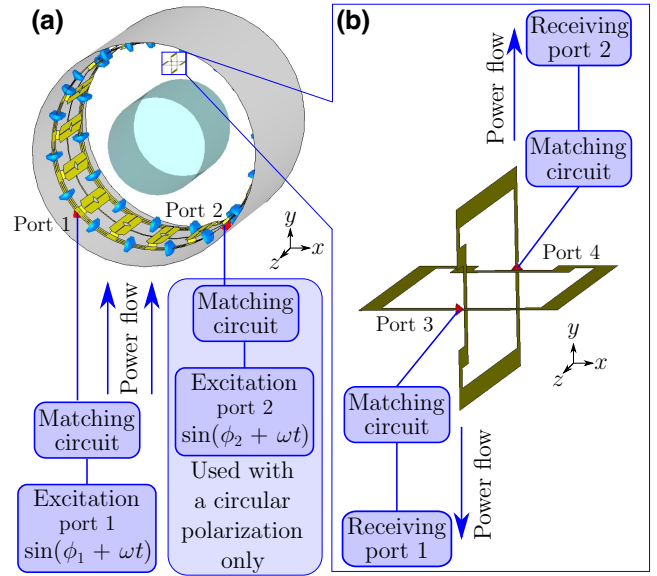


FIG. 2. (a) The schematics of WPT at a higher-order mode of a birdcage coil. The numerical model includes a birdcage coil (yellow strips), capacitors (blue), ports (red), an rf screen (gray cylinder), a phantom (blue transparent cylinder), and a receiving system (shown with the blue frame). (b) The receiving system, consisting of two orthogonal loop coils allowing us to convert horizontal and vertical polarizations of the magnetic field. The blue arrows indicate the direction of the power flows.

Finally, the model includes a WPT receiving system composed of two orthogonal loop coils, shown in Fig. 2(b). In the numerical model, we tune the resonance frequency to the value 61.67 MHz measured in our experimental setup, which is close to the Larmor frequency for 1.5-T MRI (63.55 MHz). All of the numerical simulations have been performed in CST MICROWAVE STUDIO 2022.

The receiving system consists of two identical orthogonal loop coils, namely, vertical and horizontal coils, as shown in Fig. 2(b). The loop coils are rectangular copper frames with dimensions of 100×50 mm and a width of 5 mm. The center of the receiving system is located at a height of 225 mm above the center of the birdcage [Fig. 2(a)]. Each loop in the numerical model is supplied with a single port [the red markers in Fig. 2]. Such a system allows the user to simultaneously receive the vertically and horizontally polarized linear components of the rf magnetic field and, as a result, efficiently convert circularly polarized fields [13].

The schematic block within the numerical model includes four ports: two excitation ports linked to the birdcage coil [Fig. 2(a)] and two receiving ports [Fig. 2(b)]. All four schematic ports are connected to the respective ports in models of the birdcage and receiving system through L-section matching circuits. All lumped elements in the model feature an equivalent serial resistance of 0.1Ω . In most cases, the receive and excitation ports are matched to

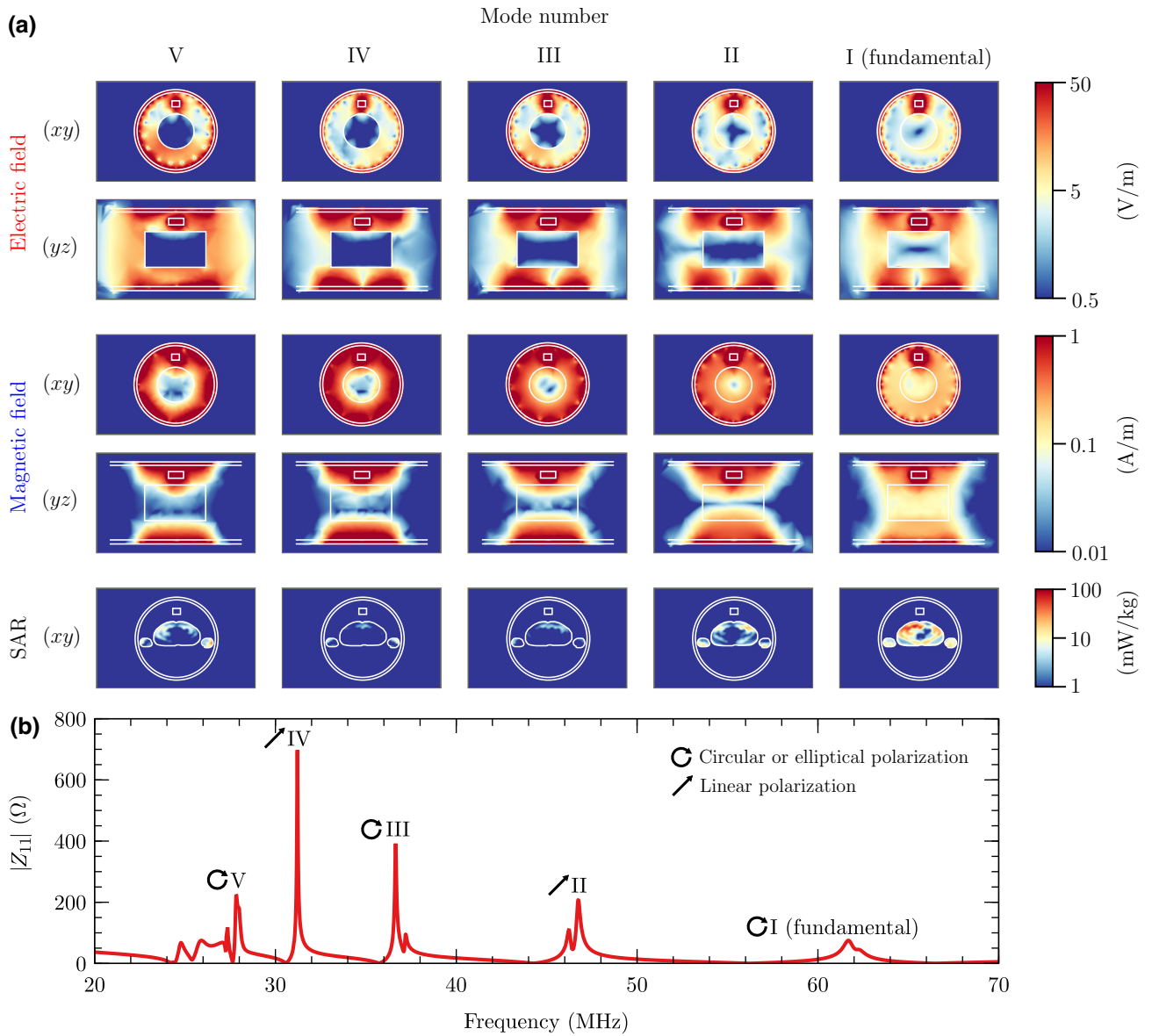


FIG. 3. (a) Numerical simulations of the electric and magnetic fields and the specific absorption rate (SAR) for different modes of the birdcage coil in the axial (x - y) and sagittal (y - z) planes. The modes are enumerated from (I) to (V), starting with the fundamental mode, which has the highest frequency. (b) The impedance spectrum (Z_{11} parameter) at the first port of the birdcage coil [Fig. 2(a)], demonstrating the characteristic resonances of different modes. The birdcage coil is considered with a cylindrical phantom (for electric and magnetic fields) and with a human voxel model (for SAR), shown with white contours. The simulations in (b) have been performed without the receiving system.

$Z = 50 \Omega$, except when calculating the resonance frequencies of the birdcage and comparing the numerical results for WPT with the experimental measurements.

III. NUMERICAL RESULTS

In our numerical simulations, we start by calculating the Z_{11} parameter of the birdcage with a body phantom for different excitation frequencies, without any receiving system, in the range from 20 MHz to 70 MHz and observe

the series of resonances shown in Fig. 3(b). The peak at 61.67 MHz corresponds to the circularly polarized fundamental mode of the birdcage used for scanning, while the peaks at lower frequencies are associated with higher-order modes. Note that while modes (III) and (V) share circular polarization, modes (II) and (IV) are linearly polarized. Due to the strong coupling between the two birdcage ports for these linearly polarized modes, we use a single port for their excitation. All of the excitation ports used are matched to 50Ω .

TABLE I. The transmitted and received power levels for the different modes of the birdcage coil, obtained in numerical simulations. The frequency of the corresponding mode is f , $P_{\text{tx}1}$ is the power transferred through the first schematic port, $P_{\text{tx}2}$ is the power transferred through the second schematic port (not applicable for linear polarization), $P_{\text{rx}1}$ is the power received by the horizontal loop, and $P_{\text{rx}2}$ is the power received by the vertical loop. The power-transfer efficiency η is calculated by Eq. (1).

Mode	f (MHz)	$P_{\text{tx}1}$ (mW)	$P_{\text{tx}2}$ (mW)	$P_{\text{rx}1}$ (mW)	$P_{\text{rx}2}$ (mW)	η (%)
(I)	61.67	500	500	34	173	20.7
(II)	46.76	1000	...	299	81	38
(III)	36.65	500	500	117	382	49.9
(IV)	31.21	1000	...	78	432	51
(V)	27.88	500	500	216	47	26.3

Next, we evaluate the distributions of the electric field, the magnetic field, and the specific absorption rate (SAR) for the birdcage excitation at the respective mode frequencies from Fig. 3(b) but now introducing the receiving system to the model [see Fig. 3(a)]. It can be seen that the magnetic fields in the axial (H_{xy}) and sagittal (H_{yz}) planes for the fundamental mode remain uniform in the phantom volume, as required for the scanning procedure, and the presence of the receiving system introduces only slight distortions in its vicinity. However, for higher-order modes, the situation is completely different: the higher the mode number, the lower is the magnetic field in the phantom. In particular, for modes (III)–(V), the magnetic field in the phantom nearly vanishes. Moreover, the frequencies of these modes significantly differ from the fundamental frequency. As a result, the power transmission at these modes will not affect the scanning procedure or create any imaging artifacts. Similar behavior is observed for the electric fields: the respective quantities vanish in

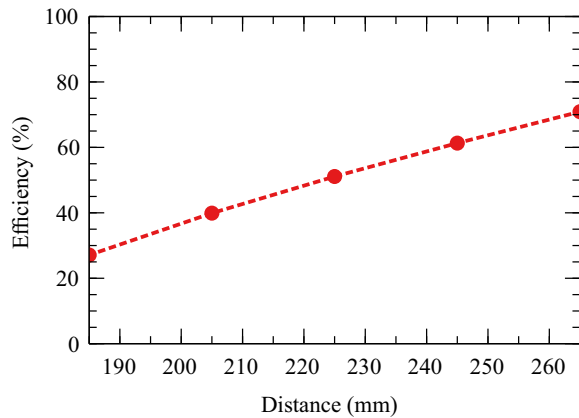


FIG. 4. The dependence of the power-transfer efficiency [see Eq. (1)] on the distance between the centers of the birdcage and the receiving system, obtained numerically. The distance is varied between 185 mm (corresponding to a separation of 10 mm between the phantom and the lower edge of the receiving system) and 265 mm (corresponding to a separation of 10 mm between the bore and the upper edge of the receiving system) in the geometry of Fig. 2(a). The distances 185 mm, 205 mm, 225 mm, 245 mm, and 265 mm are considered.

the phantom area for higher-order modes despite a pronounced electric field concentration observed at the receiving system, highlighting the safety of the proposed WPT scheme.

Next, we evaluate the rf-rf WPT efficiency at different higher-order modes (see Table I). We obtain voltages and currents at excitation ports 1 and 2 and receiving ports 1 and 2 and calculate the corresponding values of the power $P_{\text{tx}1, \text{tx}2}$ transmitted by the birdcage coil ports 1 and 2 and the power $P_{\text{rx}1, \text{rx}2}$ received by the horizontal- and vertical-loop coils of the receiving system, respectively. Then, we define the rf-rf efficiency η as

$$\eta = \frac{P_{\text{rx}1} + P_{\text{rx}2}}{P_{\text{tx}1} + P_{\text{tx}2}}. \quad (1)$$

In the case of linear polarization, the birdcage is excited with a single excitation port 1 by supplying 1000 mW, while for circular polarization both excitation ports are used and are simultaneously powered with 500 mW each. As a result, for the modes with linear polarization, $P_{\text{tx}2} = 0$. The voltage from excitation port 2 attains an additional phase of -90° . The lowest rf-rf efficiency of 20.7% is displayed by the fundamental mode, as its magnetic field is uniformly distributed in the bore volume and has low values near its edges, where the receiving system is located. Then, for higher-order modes (II)–(IV), the rf-rf efficiency monotonically grows from 38% for mode (II) and 49.9% for mode (III) to 51% for mode (IV). Such a growth is associated with an increased magnetic field localization at the bore edge (i.e., in the vicinity of the receiving system), as seen in Fig. 3(a). Then, for mode (V), the rf-rf efficiency drops to 26.3% due to a substantial increase in the electric field and an associated decrease in the magnetic field for a fixed power transmitted by the birdcage.

However, along with the transmission of an rf power, the resulting efficiency of the WPT setup is defined by the conversion of the initial dc supply to the rf signal emitted by the birdcage and a subsequent conversion of the received rf signal back to the dc one powering the load. For dc-rf conversion, the efficiencies of modern class-E power amplifiers reach 85–90% [6]. The stage of rf-dc conversion

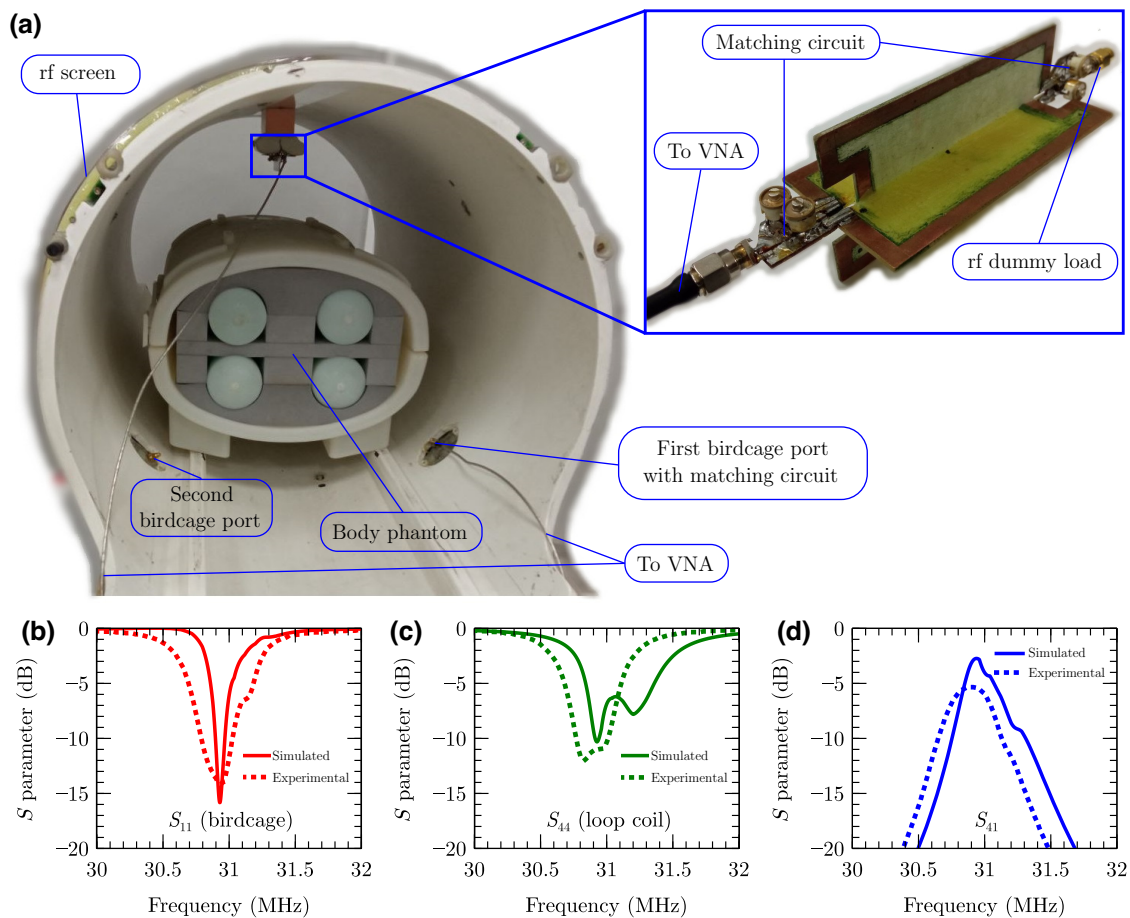


FIG. 5. (a) The experimental setup. The inset shows the receiving system. (b)–(d) A comparison of the experimentally measured (dashed lines) and numerically simulated (solid lines) S parameters: (b) the S_{11} parameter for the first port of the birdcage; (c) the S_{44} parameter for the vertical-loop antenna; and (d) the S_{41} parameter (transmission coefficient) between the first port of the birdcage and the vertical-loop antenna.

is less efficient. However, efficiencies of up to 74.4% are reported for rectifiers in the frequency range close to the considered higher-order modes [28]. Thus, the rf-rf efficiency should be multiplied by a factor of approximately 0.7 to estimate the resulting performance.

Finally, we numerically evaluate the local SAR (characterizing the local heating of the patient) [see Fig. 3(a)] and the whole-body SAR (characterizing the entire body heating). For the SAR studies, the cylindrical phantom is replaced with the Gustav voxel human model, which includes all tissues and organs and is a part of the CST BIO MODELS Library Extension. The maximum values of the local (217 mW/kg) and the whole-body (5.79 mW/kg) SAR correspond to the fundamental mode, as electric and magnetic rf fields penetrate deep into the scanning object [Fig. 3(a)]. The minimal values of the local SAR (7.8 mW/kg) and the whole-body SAR (0.299 mW/kg) correspond to modes (III) and (IV), respectively. Since MRI possesses the limitation of 2 W/kg for the local

SAR [29], the maximum achievable power at the receiving system is 128 W for mode (III) considering the center of the system, located at the height of 225 mm above the birdcage center. Such an amount allows us to fully supply common types of local receive coils [2]. The maximum received power levels are 72 W at mode (IV), 16 W at mode (II), 5 W at mode (V), and 2 W at the fundamental mode. The technical limitations for WPT with higher-order modes associated with an electromagnetic compatibility with local coils are discussed in the Supplemental Material [27].

For further studies, we select mode (IV), considering its lower SAR compared to modes (II) and (V) and the highest power-transfer efficiency among all the considered modes. Figure 4 demonstrates the dependence of the power-transfer efficiency for mode (IV) on the distance between the receiving-system center and the birdcage center. It can be seen that the efficiency increases monotonically with the distance, in accordance with the similar

growth in the magnetic field in the vicinity of the bore edge [Fig. 3(a)].

IV. EXPERIMENTAL RESULTS

To support our numerical findings, we realize WPT at mode (IV) with the help of the experimental setup shown in Fig. 5(a), which includes a birdcage coil from the Siemens Avanto 1.5 T scanner, a matching circuit for the birdcage, an rf screen made of a copper grid, a phantom, a receiving system with a matching circuit, and measurement equipment. Prior to the implementation of matching circuits for mode (IV), they have been simulated with CST MICROWAVE STUDIO 2022. The values of the capacitances and resistances in the numerical model of the birdcage coil have been obtained by measuring the components used in the experimental setup.

Figure 5 also demonstrates the S -parameters characterizing the reflection of the signal for the birdcage coil port S_{11} [Fig. 5(b)], the receiving-system port S_{44} [Fig. 5(c)], and the transmission coefficient between the birdcage and the receiving system, S_{41} [Fig. 5(d)]. It can be seen that the numerical and experimental values of the S parameters agree well, up to some broadening and the lower amplitude of the experimental peak in Fig. 5(b) which may be associated with higher losses in the experimental setup compared to the numerical model. Also, the positions of the receiving-system resonances in Fig. 5(c) appear shifted due to the high sensitivity of their positions to the values of the tuning capacitors, which may differ between the numerical simulation and the experimental setup. These results highlight the possibility of implementing such a WPT scheme in a real MRI setup.

V. CONCLUSIONS

We have demonstrated that one can implement WPT with the help of a higher-order mode of a birdcage coil. The main advantage of such an approach is the absence of an additional transmitting WPT coil and the associated power supply cables inside the MRI bore, as such metallic objects can introduce imaging artifacts. Also, the proposed solution allows the price of the WPT system to be lowered. We have studied numerically the structure of higher-order modes for a typical birdcage coil and shown that it should not introduce any imaging artifacts; we have evaluated the rf-rf power-transfer efficiency, which may reach 51%, and the maximal transmitted rf power, which is 128 W; and we have demonstrated that such an approach is safe for a patient by calculating the SAR. However, the WPT efficiency depends considerably on the location of the receiving system and the power transfer is performed only during the transmission mode, which typically takes just 0.1% of the overall working time, thus limiting the amount of transmitted power.

The future directions for developing the proposed design include incorporating the receiving system into a local coil and performing an experiment in the MRI scanner to verify that the proposed scheme does not decrease the image quality. Along with providing power for wireless multichannel coils, which require up to 100 W in the case of a 64-channel coil [2], the developed approach may find applications in powering various MRI robotic setups [22] and additional equipment such as displays, headphones, and controllers that can be used during the scanning procedure.

ACKNOWLEDGMENTS

We acknowledge fruitful discussions with Professor Stanislav Glybovski. The work is supported by the Russian Science Foundation (Project No. 21-79-30038).

-
- [1] V. Kuperman, *Magnetic Resonance Imaging: Physical Principles and Applications* (Elsevier, San Diego, 2000).
 - [2] L. Nohava, J.-C. Ginefri, G. Willoquet, E. Laistler, and R. Frass-Kriegel, Perspectives in wireless radio frequency coil development for magnetic resonance imaging, *Front. Phys.* **8**, 11 (2020).
 - [3] M. F. Dempsey and B. Condon, Thermal injuries associated with MRI, *Clin. Radiol.* **56**, 457 (2001).
 - [4] M. F. Dempsey, B. Condon, and D. M. Hadley, Investigation of the factors responsible for burns during MRI, *J. Magn. Reson. Imaging* **13**, 627 (2001).
 - [5] K. Byron, F. Robb, P. Stang, S. Vasanaawala, J. Pauly, and G. Scott, An RF-gated wireless power transfer system for wireless MRI receive arrays, *Concepts Magn. Reson. Part B Magn. Reson. Eng.* **47B**, e21360 (2017).
 - [6] K. Byron, S. A. Winkler, F. Robb, S. Vasanaawala, J. Pauly, and G. Scott, An MRI compatible RF MEMs controlled wireless power transfer system, *IEEE Trans. Microw. Theory Tech.* **67**, 1717 (2019).
 - [7] A. Ganti, J. Lin, T. Wynn, and T. Ortiz, Achieving electromagnetic compatibility of wireless power transfer antennas inside MRI system, *Wirel. Power Transf.* **6**, 138 (2019).
 - [8] S. Ullah, M. Zada, A. Basir, and H. Yoo, Wireless, battery-free, and fully implantable micro-coil system for 7 T brain MRI, *IEEE Trans. Biomed. Circuits Syst.* **16**, 430 (2022).
 - [9] A. Ganti, T. Wynn, and J. Lin, A novel energy harvesting circuit for RF surface coils in the MRI system, *IEEE Trans. Biomed. Circuits Syst.* **15**, 791 (2021).
 - [10] J. Höfflin, E. Fischer, J. Hennig, and J. G. Korvink, in *Proceedings of the International Society for Magnetic Resonance in Medicine*, Vol. 21 (Salt Lake City, Utah, USA, 2013), p. 728. https://www.researchgate.net/profile/Jens-Hoefflin-2/publication/303700956_Energy_Harvesting_towards_autonomous_MRI_detection/links/574e9e0a08ae82d2c6be32e3/Energy-Harvesting-towards-autonomous-MRI-detection.pdf.
 - [11] M. J. Riffe, J. A. Heilman, and M. A. Griswold, in *Proceedings of the International Society for Magnetic Resonance in Medicine*, Vol. 15 (Berlin, Germany, 2007), p. 3273.

- <https://cds.ismrm.org/protected/07MProceedings/PDFfiles/03273.pdf>.
- [12] M. Venkateswaran, K. Kurpad, J. E. Brown, S. Fain, and D. van der Weide, in *2020 42nd Annual International Conference of the IEEE Engineering in Medicine & Biology Society (EMBC)*, (IEEE, 2020).
- [13] P. S. Seregin, O. I. Burmistrov, G. A. Solomakha, E. I. Kretov, N. A. Olekhno, and A. P. Slobozhanyuk, Energy-harvesting coil for circularly polarized fields in magnetic resonance imaging, *Phys. Rev. Appl.* **17**, 044014 (2022).
- [14] J. I. Agbinya, *Wireless Power Transfer 2nd Edition* (CRC Press, New York, 2022).
- [15] Z. Zhang, H. Pang, A. Georgiadis, and C. Cecati, Wireless power transfer—an overview, *IEEE Trans. Ind. Electron.* **66**, 1044 (2018).
- [16] M. Song, P. Belov, and P. Kapitanova, Wireless power transfer inspired by the modern trends in electromagnetics, *Appl. Phys. Rev.* **4**, 021102 (2017).
- [17] M. Bakır, M. Karaaslan, O. Altıntaş, M. Bagmançı, V. Akdogan, and F. Temurtaş, Tunable energy harvesting on UHF bands especially for GSM frequencies, *Int. J. Microw. Wirel. Technol.* **10**, 67 (2017).
- [18] X. Hu, K. Aggarwal, M. X. Yang, K. B. Parizi, X. Xu, D. Akin, A. S. Y. Poon, and H.-S. Philip Wong, Micrometer-scale magnetic-resonance-coupled radio-frequency identification and transceivers for wireless sensors in cells, *Phys. Rev. Appl.* **8**, 014031 (2017).
- [19] R. Sharma, R. Mishra, T. Ngo, Y.-X. Guo, S. Fukami, H. Sato, H. Ohno, and H. Yang, Electrically connected spin-torque oscillators array for 2.4 GHz WiFi band transmission and energy harvesting, *Nat. Commun.* **12**, 1 (2021).
- [20] V. Palazzi, J. Hester, J. Bito, F. Alimenti, C. Kalialakis, A. Collado, P. Mezzanotte, A. Georgiadis, L. Roselli, and M. M. Tentzeris, A novel ultra-lightweight multiband rectenna on paper for RF energy harvesting in the next generation LTE bands, *IEEE Trans. Microw. Theory Tech.* **66**, 366 (2018).
- [21] S. Mutlu, O. Yasa, O. Erin, and M. Sitti, Magnetic resonance imaging-compatible optically powered miniature wireless modular Lorentz force actuators, *Adv. Sci.* **8**, 2002948 (2021).
- [22] S. Mutlu and A. Akif Kaya, Optically powered wireless and batteryless two-dimensional positioner for magnetic resonance imaging scanners, *Sens. Actuators A: Phys.* **361**, 114573 (2023).
- [23] O. Erin, M. Boyvat, J. Lazovic, M. Efe Tiryaki, and M. Sitti, Wireless MRI-powered reversible orientation-locking capsule robot, *Adv. Sci.* **8**, 2100463 (2021).
- [24] S. F. Ahmad, Y. C. Kim, I. C. Choi, and H. D. Kim, Recent progress in birdcage RF coil technology for MRI system, *Diagnostics* **10**, 1017 (2020).
- [25] J. T. Vaughan and J. R. Griffiths, *RF Coils for MRI* (John Wiley & Sons, Hoboken, NJ, USA, 2012). <https://www.wiley.com/en-us/RF+Coils+for+MRI-p-9781118590454>.
- [26] M. Rajendran, J. E. H. Yang, J. L. Kaibin, L. C. Ping, and S. Y. Huang, Birdcage transmitter for wireless power transfer, *IEEE Microw. Wirel. Compon. Lett.* **32**, 919 (2022).
- [27] See the Supplemental Material at <http://link.aps.org/supplemental/10.1103/PhysRevApplied.21.014047> for (i) detailed descriptions of the birdcage-coil schematics and the design of the experimental setup; (ii) the structure of the receiving system; (iii) the matching-circuit schematics; (iv) the local-coil electromagnetic compatibility engineering; and (v) the study of the dependence of the fundamental mode frequency on the screen diameter.
- [28] X. Zan and A. Avestruz, in *2018 IEEE Energy Conversion Congress and Exposition (ECCE)* (Portland, OR, 2018), p. 2448.
- [29] International Electrotechnical Commission, *et al.*, Medical Electrical Equipment: Particular Requirements for the Basic Safety and Essential Performance of Medical Beds, (International Electrotechnical Commission, 2015). <https://webstore.iec.ch/publication/21963>.